JOURNAL OF GEOPHYSICAL RESEARCH, VOL. 106, NO. 12, PAGES 30795–30807, DECEMBER 10, 2001

Multiparameter two-dimensional inversion of scattered teleseismic body waves 3. Application to the Cascadia 1993 data set

S. Rondenay,[1] M. G. Bostock, and J. Shragge[2]

Department of Earth and Ocean Sciences, University of British Columbia, Vancouver, British Columbia, Canada

Abstract. This is the third paper in a three-part series that examines formal inversion of the teleseismic *P* wave coda for discontinuous, two-dimensional (2-D) variations in elastic properties beneath dense arrays of three-component, broadband seismometers. In this paper, the method is applied to data from the Incorporated Research Institutions for Seismology-Program for Array Seismic Studies of the Continental Lithosphere (IRIS-PASSCAL) Cascadia 1993 experiment undertaken across central Oregon. Two major features are imaged in the resulting model. The continental Moho becomes evident ~150 km from the coast beneath the Western Cascades and extends through the eastern end of the profile at 35–40 km depth. In the western portion of the model, oceanic crust of the subducting Juan de Fuca plate dips shallowly (12°) at the coast and more steeply (27°) below the Willamette Valley and is evident to depths of >100 km beneath the High Cascades. The abrupt increase in plate dip at ~40 km depth coincides with an apparent thickening of the oceanic crust followed by a diminution in its signature. Building on previous work, we argue that these results are consistent with the consequences of prograde metamorphic reactions occurring within the oceanic crust. Progressive dehydration at lower-grade facies conditions culminates in the transformation to eclogite, producing a pronounced increase in the seismic velocity, density and dip of the subducting plate, and structural complexity in the overlying wedge.

1. Introduction

In the past few decades, numerous studies have demonstrated that a wealth of information on subsurface structure can be obtained from analysis of energy in the coda of primary teleseismic phases [e.g., *Langston*, 1979; *Owens et al.*, 1984; *Revenaugh and Jordan*, 1991; *Dueker and Sheehan*, 1997; *Bostock*, 1998]. Moreover, as the number and fidelity of recording instruments have increased, several approaches to multichannel processing of teleseismic waves that are reminiscent of migration techniques used in controlled source seismology have emerged [*Revenaugh*, 1995; *Bostock and Rondenay*, 1999; *Ryberg and Weber*, 2000; *Sheehan et al.*, 2000].

This paper is the third paper in a three-part series which investigates the inverse scattering/migration problem in earthquake seismology. The problem is set in the context of imaging lithospheric structure using the teleseismic *P* wave coda recorded on dense arrays of seismometers. The theoretical framework is developed by *Bostock et al.* [this issue] (hereinafter referred to as paper 1) and constitutes the extension of an approach suggested by *Bostock and Rondenay* [1999] (hereinafter referred to as BR) which was limited to the consideration of a strictly in-plane, two-dimensional (2-D) scattering geometry. The former study, in particular, exploits the analogy between the high-frequency, single scattering formulation of the forward problem and the generalized Radon transform [*Beylkin*, 1985; *Beylkin and Burridge*, 1990]. This analogy leads naturally to the derivation of a back projection (or approximate inverse) operator, which is tolerant of irregular source and receiver configurations, and allows for simultaneous or independent treatment of different scattering modes. Accommodation is made for incident source wave fields at arbitrary back azimuths, thereby facilitating application to field data. Moreover, the method allows for the analysis of both forward scattered and backscattered waves, the latter being afforded by free-surface reflection/conversion of the incident wave.

Shragge et al. [this issue] (hereinafter referred to as paper 2) tested the potential of the method through a series of applications involving synthetic data sets. In this paper, we focus on practical implementation of the method and its application to data from the Cascadia 1993 (CASC93) experiment [*Nabelek et al.*, 1993; *Li*, 1996]. Practical implementation is discussed in terms of (1) effect of oblique incidence on scattering kinematics and dynamics, (2) selection and weighting of different scattering modes, (3) choice of model parameterization, and (4) computational efficiency. In our treatment of CASC93, we summarize the tectonic framework and previous geophysical work in the study area and provide a brief overview of the experiment. The results of the inversion are then presented, and we conclude by discussing the implications of imaged structures for subduction zone processes in southern Cascadia.

2. Considerations for Practical Implementation

The inversion/migration technique presented in paper 1 allows for the treatment of both forward scattered (direct) and backscattered (free-surface-reflected) wave fields which are assumed to originate from a 2-D perturbation structure superposed upon a slowly varying 1-D reference medium. The strike direction of the 2-D structure is taken to parallel the x_2 coordinate. Different scattering modes are identified by index q as $q = 1$, forward scattering of incident *P* wave into *P*; $q = 2$, forward scattering of incident *P* wave into *S*; $q = 3$, free-surface-reflected *P* wave into

[1]Now at Department of Geological Sciences, Brown University, Providence, Rhode Island, USA.

[2]Now at Hager GeoScience Inc., Woburn, Massachusetts, USA.

Paper number 2000JB000039.
0148-0227/01/2000JB000039$09.00

backscattered P; q = 4, free-surface-reflected P wave into backscattered S; q = 5, free-surface-reflected S wave into backscattered P; q = 6–7, free-surface-reflected S wave into backscattered S (see also Table 1 in paper 1). There are two backscattered S-S modes, one for polarization within the plane containing the incident and scattered rays and another for polarization perpendicular to that plane. In section 2.1 we summarize expressions for travel times and amplitudes of these scattered mode combinations that are valid for plane waves obliquely incident upon 2-D heterogeneity.

2.1. Two-Dimensional Travel Times and Scattered Wave Amplitudes for Oblique Incidence

The inversion methodology requires, at each image point $\mathbf{x}$, the evaluation of several scattering potentials $g_r(\mathbf{x})$ which are defined as (see equation (39) of paper 1)

$$g_r(\mathbf{x}_0) = \frac{1}{4\pi}\int d|\mathbf{p}_\perp^0| \int d\gamma \int dx_1' \left|\frac{\partial(\psi,\ \theta)}{\partial(x_1',\gamma)}\right| \sum_q W_r^u(\theta)\frac{|\nabla_0 \mathcal{T}^q|^2}{|\mathcal{A}^q|^2} \cdot \sum_n \mathcal{A}_n^q(\mathbf{x}_0,\mathbf{x}')\, v_n^q\left[\mathbf{x}', \mathbf{p}_\perp^0, t = \mathcal{T}^q(\mathbf{x}_0,\ \mathbf{x}')\right]. \quad (1)$$

These functions are simply weighted diffraction stacks of the data $v_n^q(\mathbf{x}',\ \mathbf{p}_\perp^0,\ t\ =\ \mathcal{T}^q)$ along move out curves $\mathcal{T}^q(\mathbf{x},\ \mathbf{x}',\ \mathbf{p}_\perp^0)$ corresponding to scattering from 2-D (line) perturbations in material properties, where $\mathbf{x}' = (x_1',\ 0)$ is the receiver position along the surface and $\mathbf{p}_\perp^0 = (p_1^0, p_2)$ is the horizontal slowness of the incident wave. The radiation pattern for material parameter r and scattering mode q is defined by $W_r^q(\theta)$, and angular quantities θ, ψ, γ represent the scattering angle, dip angle, and event back azimuth, respectively. The weights include, among other factors, the product of incident and scattered wave geometrical amplitudes $\mathcal{A}_n^q$ $(\mathbf{x}, \mathbf{x}')$. We discuss the effect of obliquity on each of $\mathcal{T}^q$ $(\mathbf{x}, \mathbf{x}', \mathbf{p}_\perp^0)$ and $\mathcal{A}_n^q$ $(\mathbf{x}, \mathbf{x}')$ in turn.

2.1.1. Travel times. For convenience in processing, all travel times are normalized to the arrival of the incident P wave at each station. Expressions for the travel time curves in the in-plane case are given in paper 2. The generalizations of these expressions to incident wave fields at arbitrary back azimuths are given by

$$\mathcal{T}^{q=1,2}(\mathbf{x},\mathbf{x}',\mathbf{p}_\perp^0) = \int_0^{x_3} \frac{dy_3}{\nu^q(y_3)\sqrt{1-[\nu^q(y_3)]^2(p_1^q)^2}} - p_1^0(x_1' - x_1) - \int_0^{x_3} \frac{dy_3}{\alpha(y_3)}\sqrt{1-\alpha^2(y_3)|\mathbf{p}_\perp^0|^2}, \quad (2)$$

$$\mathcal{T}^{q=3,4}(\mathbf{x},\mathbf{x}',\mathbf{p}_\perp^0) = \int_0^{x_3} \frac{dy_3}{\nu^q(y_3)\sqrt{1-[\nu^q(y_3)]^2(p_1^q)^2}} - p_1^0(x_1' - x_1) + \int_0^{x_3} \frac{dy_3}{\alpha(y_3)}\sqrt{1-\alpha^2(y_3)|\mathbf{p}_\perp^0|^2}, \quad (3)$$

$$\mathcal{T}^{q=5,6,7}(\mathbf{x},\mathbf{x}',\mathbf{p}_\perp^0) = \int_0^{x_3} \frac{dy_3}{\nu^q(y_3)\sqrt{1-[\nu^q(y_3)]^2(p_1^q)^2}} - p_1^0(x_1' - x_1) + \int_0^{x_3} \frac{dy_3}{\beta(y_3)}\sqrt{1-\beta^2(y_3)|\mathbf{p}_\perp^0|^2}, \quad (4)$$

where

$$\nu^q(y_3) = \left[\frac{1}{\alpha^2(y_3)} - (p_2)^2\right]^{-\frac{1}{2}}, \qquad q = 1,3,5, \quad (5)$$

$$\nu^q(y_3) = \left[\frac{1}{\beta^2(y_3)} - (p_2)^2\right]^{-\frac{1}{2}}, \qquad q = 2,4,6,7. \quad (6)$$

The quantity $\nu^q(y_3)$ can be interpreted as an obliquity-corrected velocity at depth y_3 in the reference medium, and p_1^q is the component of the scattered wave slowness in the x_1 direction ($p_1^q = p_1^P$ for q = 1,3,5; and $p_1^q = p_1^S$ for q = 2,4,6,7). Since p_2 is constant across all scattered waves for any individual, incident wave field, there is no travel time dependence on x_2 in (2)–(6), and so the calculations are performed entirely with respect to spatial coordinates x_1 and x_3.

2.1.2. Scattered wave amplitude. The effect of obliquity on the product of amplitudes, $\mathcal{A}_n^q(\mathbf{x},\ \mathbf{x}')$, is contained entirely within the amplitude of the Green's function since the incident wave field is planar with an amplitude that depends only on the material properties (e.g., equation (21) of paper 1). Thus the amplitude of the 2-D, P wave Green's function corresponding to a line source with axial component of forcing is expressed as (see paper 1, Appendix A and Figures 4 and A1)

$$A^P(x_3; x_3'; p_2) = \frac{1}{4\alpha(x_3')}\sqrt{\frac{2}{\pi\rho(x_3)\alpha(x_3)\rho(x_3')[J^P(x_3;x_3')]^2\sqrt{1-p_2^2\alpha^2(x_3')}}}, \quad (7)$$

where ρ is the density, and the geometrical spreading for the 1-D reference medium is given by

$$J^P(x_3;x_3') = \sqrt{\frac{\cos\phi(x_3)\cos\phi(x_3')}{\nu^q(x_3)}\left(\frac{\partial x_1'}{\partial p_1^P}\right)}. \quad (8)$$

The quantity ϕ is the angle between the ray and the vertical projected into the x_1-x_3 plane. Obliquity is evident in (7) through the factor $\sqrt{1-p_2^2\alpha^2(x_3')}$ in the denominator and in (8) through the obliquity-corrected velocity $\nu^q(x_3)$. Corresponding expressions for the scattered S wave are obtained by replacing α by β and superscript P by S in (7) and (8).

2.2. Interpolation

In practice, the quantities presented in section 2.1 (i.e., $\mathcal{T}^q(\mathbf{x},\mathbf{x}',\ \mathbf{p}_\perp^0)$, $\nu^q(x_3)$, $J^P(x_3;x_3')$, and p_1^q) will need to be computed at every image point (x_1, x_3) for multiple sources (as identified by the horizontal slowness $|\mathbf{p}_\perp^0|$ of the incident wave) and multiple receivers (as identified through surface coordinate x_1'). To minimize the computational burden, a set of tables containing travel time and geometrical spreading parameters for a regularly sampled range of $(x_1 - x_1')$, x_3, p_1^0, and p_2 are computed in advance using the 1-D reference velocity model. During inversion the required quantities are recovered through table lookup and interpolation, thereby reducing computing time substantially.

2.3. Inversion

As discussed in papers 1 and 2, several factors may influence the recovery of material property perturbations in the inversion. These factors include the effect of parameter choice on the conditioning of the problem, the selection and relative weighting of mode interactions, q, included in the inversion, and the choice of Jacobian for the irregular, sparse distribution of global seismicity.

2.3.1. Choice of inversion parameters. As the forward problem in paper 1 is developed for purely isotropic heterogeneity, the material property perturbations can be expressed in terms of three independent parameters. Examples of physically meaningful parameter combinations include the Lamé constants and density ($\Delta\lambda/\lambda$, $\Delta\mu/\mu$, $\Delta\rho/\rho$), elastic wave velocities and density ($\Delta\alpha/\alpha$, $\Delta\beta/\beta$, $\Delta\rho/\rho$), or impedances and density ($\Delta I_P/I_P$, $\Delta I_S/I_S$, $\Delta\rho/\rho$). However, the optimal choice, as dictated by the

condition number of the inverse problem, may not correspond to these simple forms and must be determined through eigenvector analysis for general experimental configurations [*Forgues and Lambaré*, 1997]. For inversion of the Oregon data set we shall employ a reduced parameter set comprising P and S velocity perturbations. Density perturbations are not considered as they are effectively indeterminate for realistic array geometries and noise conditions. We further note that although velocities are an appropriate set of independent variables for forward scattering, impedances are favored for backscattered waves. As our approach involves a mixture of scattering modes, we shall adopt velocities largely as a matter of convenience, recognizing that they may not be optimal.

2.3.2. Choice of scattering modes. An advantage of our approach is the ability to simultaneously consider multiple scattering modes which leads to improved resolution of structure (see paper 2). A natural relative weighting for different mode interactions enters (1) through the factor $|\nabla \mathcal{T}^q|^2$, which is a measure of the sensitivity of a particular mode's travel time to structural location. As a result, it can be shown (see paper 1) that forward scattering interactions are less sensitive to structure than backscattering interactions, a situation which is particularly acute for the P-P (q = 1) mode. However, it should also be noted that the derivation of (1) assumes a complete isolation of the different modes. This requirement can be only partially realized in practice through the approximate orthogonality of P and S wave polarizations. Consequently, different mode interactions cross contaminate one another to different degrees with relative amplitudes that are controlled in part by the strength of free-surface reflection/conversion coefficients for a particular incident wave. For example, backscattered S-P (q = 5) energy is, in most cases, considerably weaker than that of backscattered P-P (q = 3), as a result of two consecutive conversions. Therefore it is desirable to further weight contributions according to their relative signal amplitudes. On the basis of these considerations we will refrain from using modes q = 1, 5 in our simultaneous inversion. Moreover, we shall weight contributions from the remaining modes (q = 2, 3, 4, 6, 7) on the basis of signal recovery determined from individual-mode inversions (see section 4.5).

2.3.3. Choice of Jacobian. Another issue requiring consideration involves the choice of Jacobian in (1), which is employed in transforming the integration over geometrical quantities (ψ, θ) to one involving the experimental variables (i.e., sources and receivers). This Jacobian can take several forms since there are at least three experimental variables. The source variable in the Jacobian can be represented through either the magnitude of horizontal slowness ($|\mathbf{p}_\perp^0|$) or the event back azimuth (γ). In special cases where structural recovery is limited to a single material parameter, angle θ no longer needs to be considered in the transformation of variables, and the Jacobian reduces to a simple derivative (see equation (B11) in paper 1). The preferred choice of Jacobian will thus be governed by the distribution of seismicity and the selection of inversion parameters. For the CASC93 data set we employ equation (B10) in paper 1 for P-P scattering to avoid downweighting sources which are close to in-plane ($p_2 \approx 0$) and yield a null Jacobian in equation (B9) of paper 1. In the case of P-S and S-S scattering, we employ the single-parameter Jacobian because the perturbation in S velocity ($\delta\beta/\beta$) is the sole inversion parameter for those modes.

3. Preprocessing of the Data

Prior to inversion the raw data must be preprocessed to effectively remove the incident wave field, thereby isolating the scattered displacement field (i.e., $\Delta u_i(\mathbf{x}')$ in equation (5) of paper 1). This preprocessing involves several steps which are presented in detail by BR and can be summarized as (1) transform displacement to a wave vector space using the free-surface transfer matrix [*Kennett*, 1991] to isolate the incident P wave; (2) time normalize the resulting P wave section using multichannel cross-correlation-derived delay times [*VanDecar and Crosson*, 1990]; (3) estimate and separate incident and scattered wave fields by principal component analysis of the P wave section [*Ulrych et al.*, 1999]; (4) reconstitute scattered displacement using the inverse free-surface transfer matrix; (5) deconvolve source-time function (estimated from the first or first few principal components) from recovered displacement sections; (6) rotate horizontal displacement into a reference frame aligned with the inferred strike of the study area (i.e., x_2 parallel to 2-D regional strike); and (7) apply the filter $\mathcal{F}(\omega) = -i\,\mathrm{sgn}(\omega)/\sqrt{-i\omega}$ to the scattered displacement. This final operation yields the quantity $v_n^q(\mathbf{x}', \mathbf{p}_\perp^0, t)$, which appears in equation (1).

4. Application to CASC93

To date, few passive seismic experiments have employed array configurations suitable for multichannel processing of scattered waves as envisaged here. However, during 1993–1994, researchers at Oregon State University undertook the Incorporated Research Institutions for Seismology-Program for Array Seismic Studies of the Continental Lithosphere (IRIS-PASSCAL) CASC93 experiment with the objective of imaging detailed structure of the Cascadia subduction zone across central Oregon [*Nabelek et al.*, 1993]. This deployment was unprecedented in both number and density of receivers, and thus it presents an ideal opportunity to gauge the performance of our algorithm on an actual field data set. We precede our treatment of CASC93 with an overview of tectonics in the Cascadia subduction zone and previous geophysical work.

4.1. Tectonic Framework

The Cascadia subduction zone extends along the west coast of North America, from southern British Columbia to northern California (Figure 1), and involves subduction of the Juan de Fuca plate beneath the North American plate at a rate of ~42 mm/yr in a direction approximately N69°E [*DeMets et al.*, 1990]. Along the trench, the plate is relatively young (i.e., 4–10 Myr) and warm [*Heaton and Hartzell*, 1987; *Hyndman and Wang*, 1993].

The region sampled by the CASC93 experiment represents a record of past and present accretionary events along the western North American Cordillera and extends from the coast of central Oregon well into the back arc. The surface geology includes, from west to east, (1) the Coast Ranges, composed of seamounts and oceanic basalt terranes accreted to North America during Paleocene to middle Eocene and subsequently covered by marine forearc sediments (these structures are collectively defined as the Siletz terrane by *Tréhu et al.* [1994] and were uplifted in the west during late Eocene to Oligocene in response to continued underthrusting by the Juan de Fuca plate [*Christiansen et al.*, 1992]); (2) the Willamette Valley, a structural trough within the Siletz terrane, covered with thick sequences of middle Tertiary to Quaternary sediments [*Tréhu et al.*, 1994]; (3) the Cascade Range, which is a result of continental arc volcanism related to the subduction of the Juan de Fuca plate in the Tertiary (Western Cascades) and Quaternary (High Cascades); and (4) the Columbia Intermontane, or back arc, region composing various structural basins filled with Miocene to Quaternary volcanic and sedimentary strata. These basins form high-elevation plateaus (e.g., Columbia Plateau, High Lava Plains), separated in central Oregon by Late Triassic to Early Cretaceous accreted terranes forming the

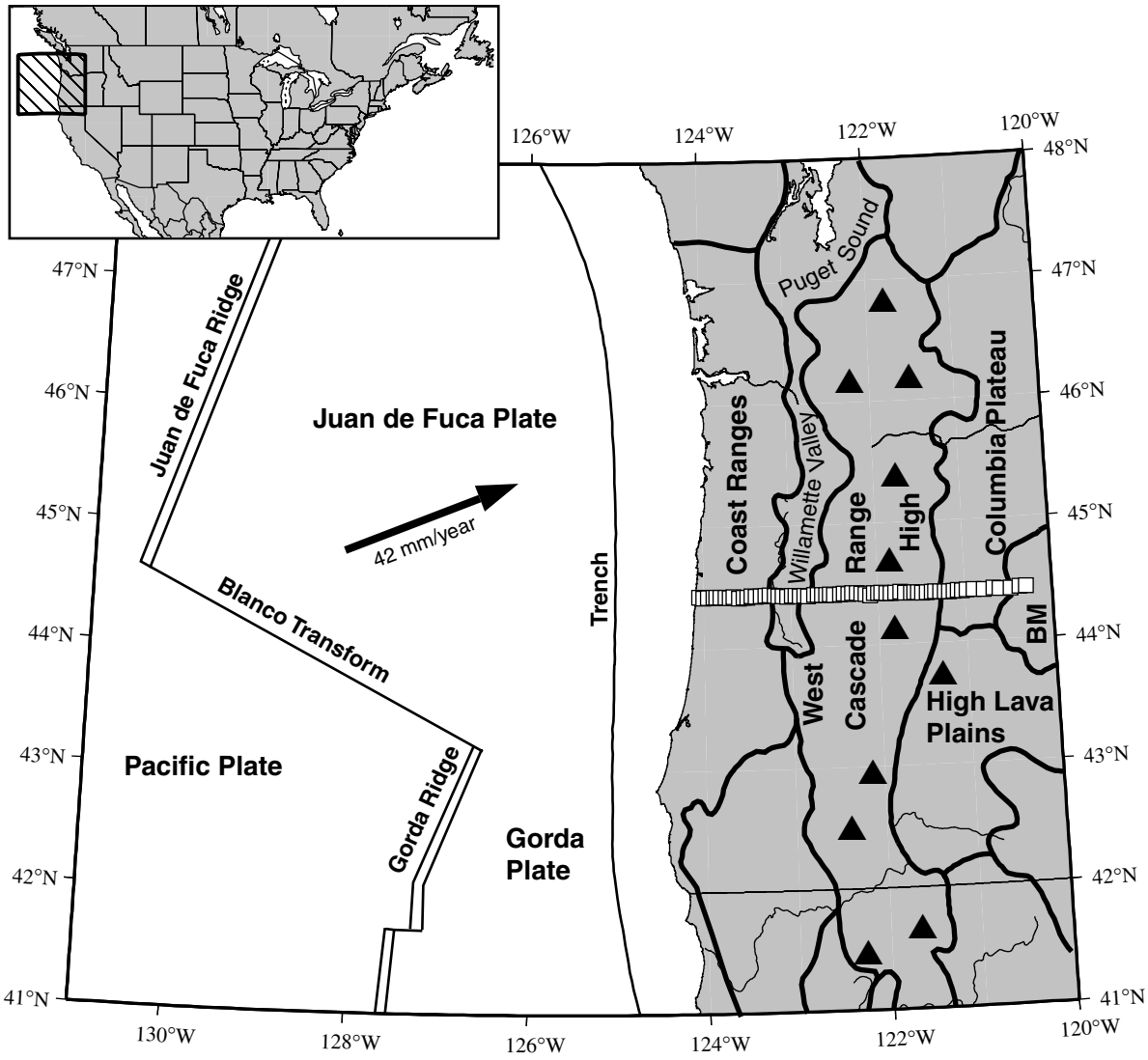

Figure 1. Simplified tectonic map of the Cascadia subduction zone in western Oregon and Washington (modified from *Mooney and Weaver* [1989]), with location of the CASC93 teleseismic stations indicated by open squares. Arrow indicates the direction of convergence of the Juan de Fuca plate relative to North America. Solid triangles mark the position of High Cascades stratovolcanoes. Inset shows the location of the study area with respect to North America.

Blue Mountains [*Mooney and Weaver*, 1989; *Christiansen et al.*, 1992].

4.2. Previous Geophysical Studies

A variety of geophysical studies have been undertaken to image the Cascadia subduction zone beneath central Oregon. These include a major magnetotelluric survey [*EMSLAB Group*, 1988; *Wannamaker et al.*, 1989], a series of controlled and passive source seismic studies [e.g., *Langston*, 1981; *Michaelson and Weaver*, 1986; *Rasmussen and Humphreys*, 1988; *Keach et al.*, 1989; *Harris et al.*, 1991; *VanDecar*, 1991; *Nabelek et al.*, 1993; *Tréhu et al.*, 1994; *Li*, 1996; *Flueh et al.*, 1998], and potential field modeling [*Couch and Riddihough*, 1989; *Fleming and Tréhu*, 1999]. Some of the first geophysical evidence for the subducting Juan de Fuca plate beneath central Oregon was provided by *Langston* [1981], using receiver function analysis at World-Wide Standardized Seismograph Network (WWSSN) station COR (Corvallis, Oregon). This study identified the Moho of the subducting oceanic lithosphere as the base of a low-velocity zone 45–50 km beneath the station, dipping eastward at 20°.

Wannamaker et al. [1989] modeled magnetotelluric data from the EMSLAB experiment to image the subducting oceanic crust of the Juan de Fuca plate as a ~5-km-thick conductive layer dipping at ~20° and extending to ~60 km depth below the Willamette Valley. They interpreted high conductivity at shallower levels as due to the presence of fluids within the subducting crust. Farther inland, they identified a second, more conductive, horizon above the dipping plate, starting in the lower crust and upper mantle beneath the Willamette Valley and extending eastward. This conductive body was interpreted as a region of trapped fluids expelled from the oceanic crust as a result of dehydration/devolatilization accompanying high-pressure and high-temperature metamorphic reactions.

Controlled-source, seismic surveys using refracted phases and wide-angle reflections [*Tréhu et al.*, 1994] also image the

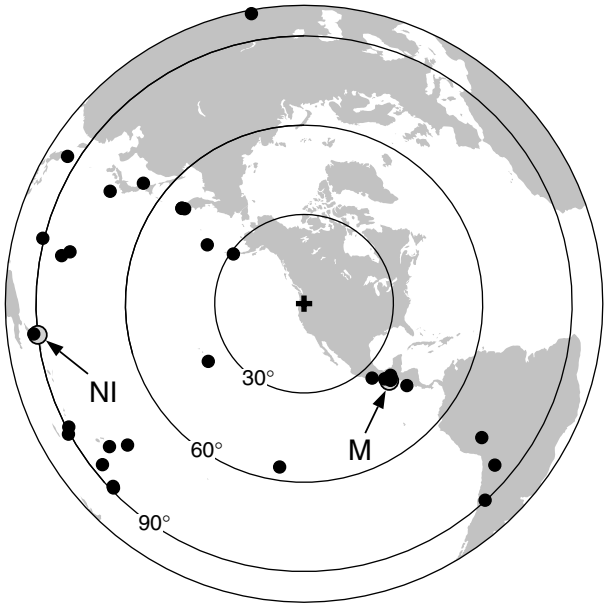

Figure 2. Distribution of events selected for multichannel inversion. M and NI denote events from Mexico (event 15 in Table 1) and New Ireland region (event 16 in Table 1), respectively, retained for detailed analysis in the text.

subducting Juan de Fuca crust beneath the forearc, both offshore [*Flueh et al.*, 1998] and to greater depth on land. Tréhu et al. identified the oceanic crust as a 5- to 8-km-thick low-velocity layer dipping at 13–16° beneath the Coast Ranges. Moreover, they observed a progressive thickening of the upper crust with increasing depth along the subduction zone. This thickening was associated with a series of strong reflectors at 30–40 km depth (originally identified by *Keach et al.* [1989]) that were tentatively interpreted as the incorporation of a block of oceanic crust within the accretionary prism [*Tréhu et al.*, 1994]. The results of *Tréhu et al.* [1994] were used to constrain models of magnetic and gravity anomalies for the offshore portion of the subduction zone in central Oregon [*Fleming and Tréhu*, 1999]. These models indicate that the sedimentary column entering the subduction zone has a maximum thickness of 2 km, in close agreement with the estimates of *Flueh et al.* [1998]. Furthermore, demagnetization of subducting oceanic crust has been inferred to occur beneath the continental shelf. *Fleming and Tréhu* [1999] suggest that this is caused, in part, by increased hydrothermal alteration and metamorphic reactions.

Using receiver function analysis and constraints from the crustal velocity model of *Tréhu et al.* [1994], *Li* [1996] provided an interpretation of the CASC93 data set and modern digital data from station COR. He identified direct and multiple *P*-to-*S* conversions from the oceanic crust (modeled as an ~7-km-thick low-velocity layer) which were interpreted to indicate an increase in dip of the subducting plate from 10° beneath the Coast Ranges to 23° beneath the Willamette Valley and the Western Cascades. The continental Moho was modeled at 35–40 km depth beneath the eastern portion of the array, starting ~150 km from the coast. Poisson's ratio estimates for the crust vary laterally through the model, with values of 0.33 beneath the Coast Ranges, 0.25 beneath the Willamette Valley and the Cascades, and 0.27 in the back arc [*Li*, 1996].

Several *P* wave, travel time tomography studies have been performed in the Pacific Northwest to investigate the deeper structure of the Cascadia subduction zone [*Michaelson and Weaver*, 1986; *Rasmussen and Humphreys*, 1988; *Harris et al.*, 1991; *VanDecar*, 1991]. These studies image the subducted Juan de Fuca plate in the upper mantle beneath the High Cascades as a steeply dipping tabular feature ~100 km thick and characterized by velocities that are 2–4% faster than the surrounding mantle. The anomaly persists to ~300 km depth beneath central Washington and northern Oregon but only to 150–200 km depth beneath central and southern Oregon. The loss in signature below these depths is interpreted as either a change in thermal/compositional properties that reduces the velocity contrast between the slab and the surrounding mantle [*Rasmussen and Humphreys*, 1988] or a tear in the slab related to changes in subduction rate over the past ~10 Myr [*VanDecar*, 1991].

Finally, it is worth noting that the southern Cascadia subduction zone is characterized by abnormally low crustal seismicity in the continental forearc relative to more northerly latitudes [*Weaver and Michaelson*, 1985] and a virtual absence of Wadati-Benioff seismicity. *Weaver and Michaelson* [1985] interpret this variation in seismicity as indicative of a segmentation of the Juan de Fuca plate, whereby the southern portion of the slab is quasi-planar and less coupled to the overriding plate and has a higher dip angle (past the arc) than the northern portion.

4.3. Experiment and Data Set

The CASC93 data set was acquired using 44 portable RefTek data loggers and Guralp-ESP/STS-2 three-component broadband seismometers, deployed in several phases [*Li*, 1996]. Stations were relocated several times during the 1-year period, for a total of 69 sites and an average station spacing of ~5 km [*Li*, 1996]. Between February and April 1994, fewer than 15 stations were operational, resulting in limited data coverage along the easternmost portion of the array.

The selection of data for multichannel inversion was performed qualitatively, with the requirement that traces show high signal-to-noise ratio for incident *P* waves and converted *S* and *P* phases following in the *P* coda. Figure 2 illustrates the final event distribution on a polar projection centered on the array. All events (see Table 1) fall between 30° and 104° epicentral distance to avoid transition zone triplications and core diffracted *P*. This selection resulted in an average of 32 station recordings per event after removal of individual, low-quality traces. Back azimuthal coverage is governed by the global distribution of plate boundaries, and events evenly span most of the second, third, and fourth quadrants (as measured clockwise from north), although there is no representation between 0° and ~120°.

The choice of strike direction (i.e., x_2) for the 2-D inversion is facilitated by the observation that the main surface features (i.e., deformation front, Willamette Valley, High Cascades) all run approximately north-south. Thus we set x_1 and x_2 to coincide with due east and due south, respectively. Figure 3 displays a series of three-component preprocessed data sections for two events situated in Mexico and the New Ireland region (events 16 and 15 in Table 1, respectively), with incident waves illuminating subsurface structure obliquely from the right and left, respectively. Examples of travel time curves $\mathcal{T}^q(\mathbf{x}, \mathbf{x}', \mathbf{p}_\perp^0)$ for a scatterer located at −122.55° and 55 km depth are superposed upon the data sections. These events were selected to illustrate the dependence of scattered response on direction of source incidence (see paper 2 for discussion). In the case of the Mexico earthquake the most striking features are a series of dipping conversions observed over the western portion of the array. The first of these is a forward scattered wave ($q = 2$) from the subducted plate, which arrives between 5 and 10 s after direct *P*. It is followed by a lower-frequency backscattered ($q = 4$) arrival between 10 and 30 s. In the eastern portion of the array, between −121.2° and −122.3° (i.e.,

Table 1. Events Selected for Multichannel Inversion[a]

Event	Date	Time, UT	Lat, °N	Lon, °E	Depth, km	m_b	NS	$q = 2$	$q = 3$	$q = 4$	$q = 6,7$
1	May 15, 1993	2152:25	51.37	−178.67	32	6.2	26			X	X
2	May 16, 1993	2144:48	−15.29	−173.33	21	6.1	31			X	X
3	May 17, 1993	1602:53	−5.34	151.99	17	5.7	30			X	X
4	May 18, 1993	1019:33	19.91	122.45	169	6.4	30			X	X
5	May 24, 1993	2351:28	−22.67	−66.54	221	6.6	38		X	X	X
6	June 6, 1993	1323:20	15.82	146.60	14	6.0	36			X	X
7	June 8, 1993	1303:36	51.22	157.83	71	6.4	33			X	
8	June 8, 1993	2317:41	−31.56	−69.23	113	6.5	37		X	X	X
9	June 18, 1993	1152:51	−29.05	−176.75	16	6.2	38			X	X
10	June 18, 1993	1757:46	−28.68	−176.89	11	5.9	38			X	X
11	Aug. 7, 1993	1753:24	−23.87	179.85	523	6.0	38			X	X
12	Aug. 7, 1993	1942:41	41.99	139.84	14	6.2	38			X	X
13	Aug. 9, 1993	1242:48	36.38	70.87	215	6.2	38		X	X	X
14	Aug. 11, 1993	1417:37	13.18	145.65	22	5.9	36		X	X	X
15	Sept. 3, 1993	1235:00	14.52	−92.71	27	5.8	41	X	X	X	X
16	Sept. 6, 1993	0356:00	−4.64	153.23	49	6.2	39			X	X
17	Sept. 10, 1993	1728:08	14.43	−92.81	62	5.3	38	X	X	X	X
18	Sept. 10, 1993	1912:54	14.72	−92.64	34	6.2	40	X	X	X	X
19	Sept. 19, 1993	1410:56	14.36	−93.32	18	5.7	43	X	X	X	X
20	Sept. 26, 1993	0331:14	10.00	138.22	10	6.1	40			X	X
21	Sept. 30, 1993	1827:50	15.42	−94.70	19	5.8	44	X	X	X	X
22	Oct. 11, 1993	1554:21	32.02	137.83	351	6.4	41			X	X
23	Oct. 24, 1993	0752:15	16.75	−98.72	21	6.3	35	X	X	X	X
24	Nov. 13, 1993	0118:04	51.93	158.65	34	6.5	40			X	X
25	Jan. 10, 1994	1553:50	−13.34	−69.45	596	6.4	4			X	X
26	Feb. 11, 1994	2117:31	−18.77	169.17	206	6.4	14			X	X
27	Feb. 12, 1994	0416:26	−10.79	−128.80	15	6.3	15	X		X	X
28	Feb. 12, 1994	1758:24	−20.56	169.33	28	6.3	15			X	X
29	March 9, 1994	2328:06	−18.04	−178.41	563	6.6	13			X	X
30	March 14, 1994	2051:24	15.99	−92.43	164	5.8	13	X		X	X
31	March 15, 1994	0336:19	11.11	−88.08	15	5.8	13	X		X	X

[a] Event latitude, longitude, and magnitude are denoted by Lat, Lon, and m_b, respectively. NS denotes the number of station recordings per event, and crosses mark scattering modes (q = 2, 3, 4, 6, 7) retained for simultaneous inversion.

150–275 km east of the coast) a series of laterally coherent arrivals at ~4–6 s represent a forward scattered wave (q = 2) from the continental Moho. For the New Ireland event the direct conversion (q = 2) is largely absent in the western portion of the array, while the reverberation (q = 4) is again observed between 10 and 30 s, as is the near-horizontal Moho signal in the east. The conversions in this case are strongest on the Δu_1 profile, as the incident wave field arrives nearly in plane; thus Δu_1 corresponds approximately to the radial component.

4.4. Reference Model

Our approach to inversion is based on the single-scattering or Born approximation which is valid for small-contrast material property perturbations defined with respect to a 1-D reference model (paper 1). It is important therefore to select a broadly representative reference model if structural features are to be accurately imaged. We constructed a 1-D S velocity model adapted from both the 1-D (COR) and 2-D (CASC93) modeling results of *Li* [1996], which is presented in Table 2. To compute P velocities, we employ a constant Poisson's ratio of 0.33 for the crust, consistent with the value inferred by *Langston* [1979] and *Li* [1996] in the western portion of the model and a value of 0.3 for the mantle [*Holbrook et al.*, 1992].

4.5. Results

All inversions were performed for a 2-D model discretized at 2-km intervals in the x_1 and x_3 directions. We begin by presenting inversion results for individual events and scattering modes in order to identify their contributions to the final model. Figure 4 displays the results for the New Ireland and Mexico events (see Figure 2 for location), with the gray scale representing negative (slower) to positive (faster) velocity perturbations as white to black, respectively. The most prominent feature observed in single-mode inversions is a dipping, low-velocity tabular feature in the western portion of the model, associated with the subducting Juan de Fuca plate (see, in particular, Figure 4c–4h). Results for (q = 4) inversions (i.e., Figure 4c and 4g) further image a horizontal discontinuity in the central/eastern portion of the profile, marking a jump from low to high velocity at deeper levels and inferred to represent the continental Moho. As a result of their relative signal levels, these two features are not equally well resolved within the individual-mode inversions. For example, the (q = 2) inversion does not recover the Juan de Fuca slab when illuminated from the left (Figure 4a) because of near-normal incidence of the direct P wave. Backscattered P-P inversion for the same event also displays a poor recovery of structure; however, this may be due to a loss of low-frequency P-P scattered signal to the estimated source-time function during preprocessing.

Although not shown here, comparable analyses have been conducted for all individual events. This exercise was useful in devising a weighting strategy for individual event-mode combinations within the simultaneous inversion. The intent of the weighting is to reduce the contributions from scattering modes that display a weak or null response. Only modes that recovered some signature of the two main structures (i.e., Juan de Fuca crust and continental Moho) were retained for simultaneous inversion (see Table 1). In general, structural recovery was consistently poorer for inversions involving q = 2, 3 than those for q = 4, 6, 7;

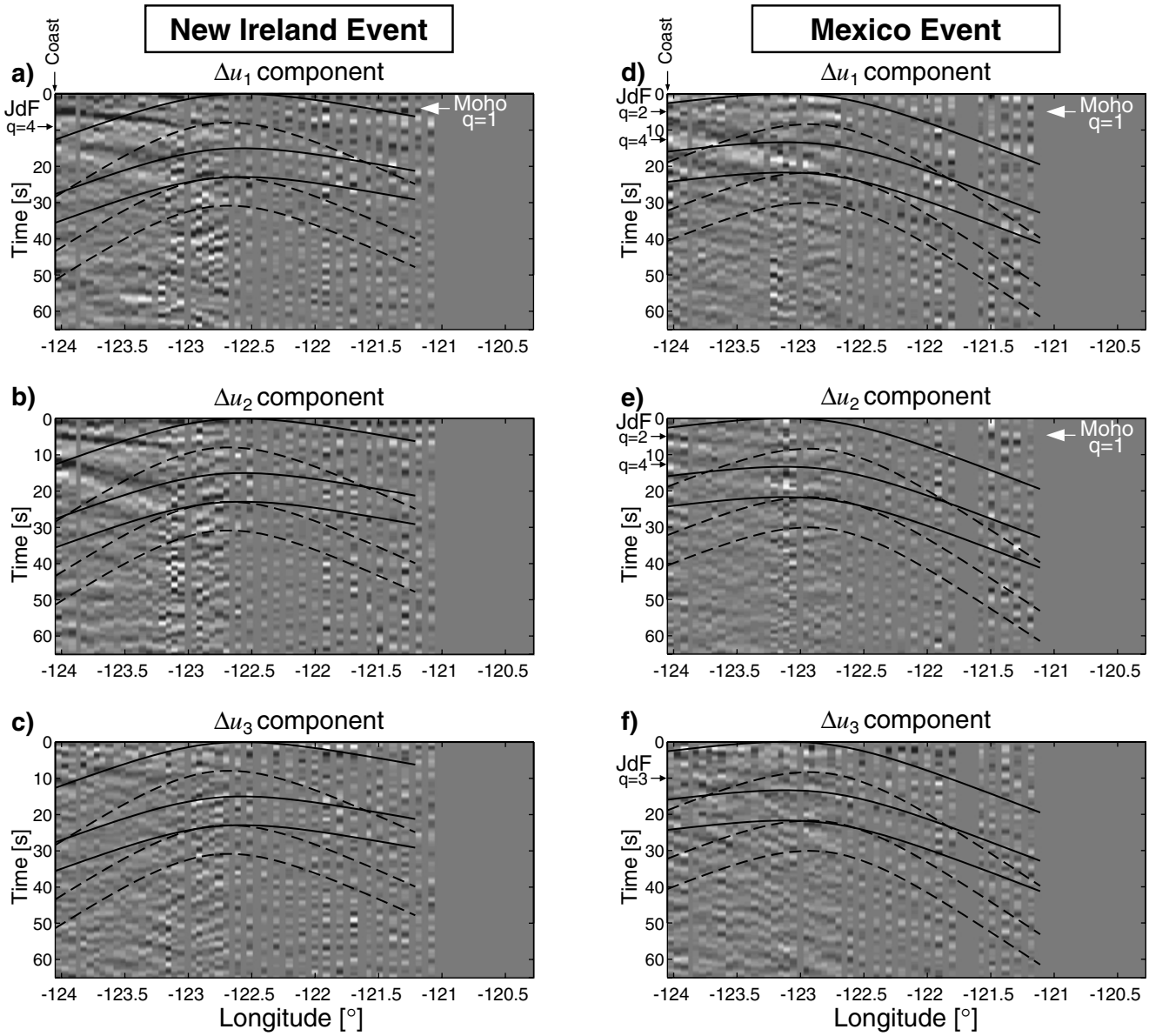

Figure 3. Three-component preprocessed data sections for events M and NI (Figure 2). Diffraction hyperbolas ($\mathcal{T}^q(\mathbf{x}, \mathbf{x}', \mathbf{p}_\perp^0)$ in equations (2)–(4) are plotted on each section and identified as (from top to bottom) solid lines for q = 1, 3, 5 and dashed lines for q = 2, 4, 6–7. Arrows point to main conversions from the Juan de Fuca (JdF) plate and continental Moho.

consequently, the latter group were somewhat arbitrarily upweighted by a factor of 10. A more objective basis for relative weighting of scattering contributions will be the topic of future research.

Simultaneous inversion of all events listed in Table 1 was performed using a selection of scattering modes. Individual scattering-mode images are presented in Figure 5 and show an appreciable improvement in reconstruction over those of the single-event inversions (Figure 4). Resulting P and S velocity perturbation models for the multimode, multievent inversion are displayed in Plate 1 with a red to blue color scale representing negative (slower) to positive (faster) velocity perturbations. The receiver function model of *Li* [1996] is superposed on our profile in Plates 1c and 1d for comparison. A good correlation is observed between the two models. The dipping, low-velocity layer in the western portion of the array has been interpreted by *Li* [1996] as the oceanic crust of the Juan de Fuca plate sandwiched between high-velocity mafic and ultramafic material of the overriding plate and oceanic mantle, respectively. In our model this layer is well defined from 20 km depth beneath the coast to 40 km depth beneath the Willamette Valley, with a dip of ∼12° and an average thickness near 10 km. Below 40 km, the signature of the oceanic crust becomes noticeably weaker. The oceanic Moho, however, persists to at least 100 km depth, dipping more steeply at ∼27°. The continental Moho is imaged at 35–40 km depth from −122.3° (i.e., 150 km east of the coast) to the eastern edge of the model.

An interesting feature in our profile is the disruption of oceanic crust at ∼40 km depth below the Willamette Valley,

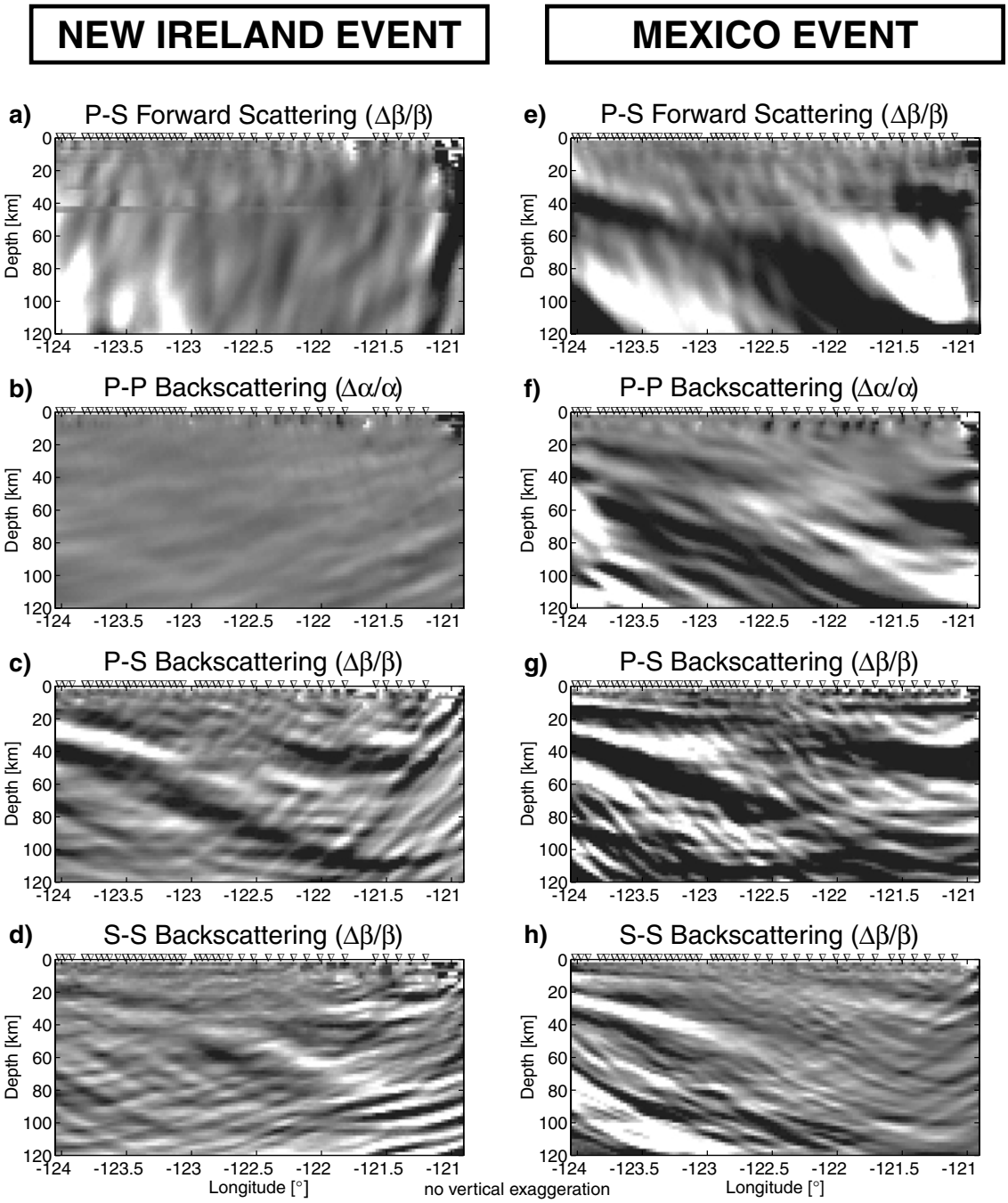

Figure 4. Results from single scattering-mode inversion of events M and NI (Figure 2). Gray scale indicates slow (white) and fast (black) seismic velocity perturbations.

which accompanies the change in dip and signature of the subducting oceanic crust. While this transition in dip is modeled as a simple "elbow" in the receiver function analysis of *Li* [1996], it appears here to be associated with a local thickening of the effective low-velocity layer and a possible bifurcation of the crust or plate. While we acknowledge the potential for contamination by unaccounted for extraplanar structure, we believe that the appearance of deviations from a simple slab bend within the image plane is real. In particular, we note that the upper portion of this feature, situated at ~30 km beneath the Willamette Valley, coincides with the zone of high reflectivity and increased thickness inferred from con-

Table 2. Reference 1-D Velocity Model for Multichannel Inversion of the CASC93 Data Set

Layer	Depth, km	α, km/s	β, km/s	ρ, g/cm^3
1	0–5	5.50	2.77	2.6
2	5–8	6.35	3.20	2.6
3	8–11	6.47	3.26	2.6
4	11–16	6.67	3.36	2.9
5	16–21	6.75	3.40	3.1
6	21–25	6.93	3.49	3.1
7	25–40	7.16	3.61	3.1
8	40–300	8.10	4.33	3.5

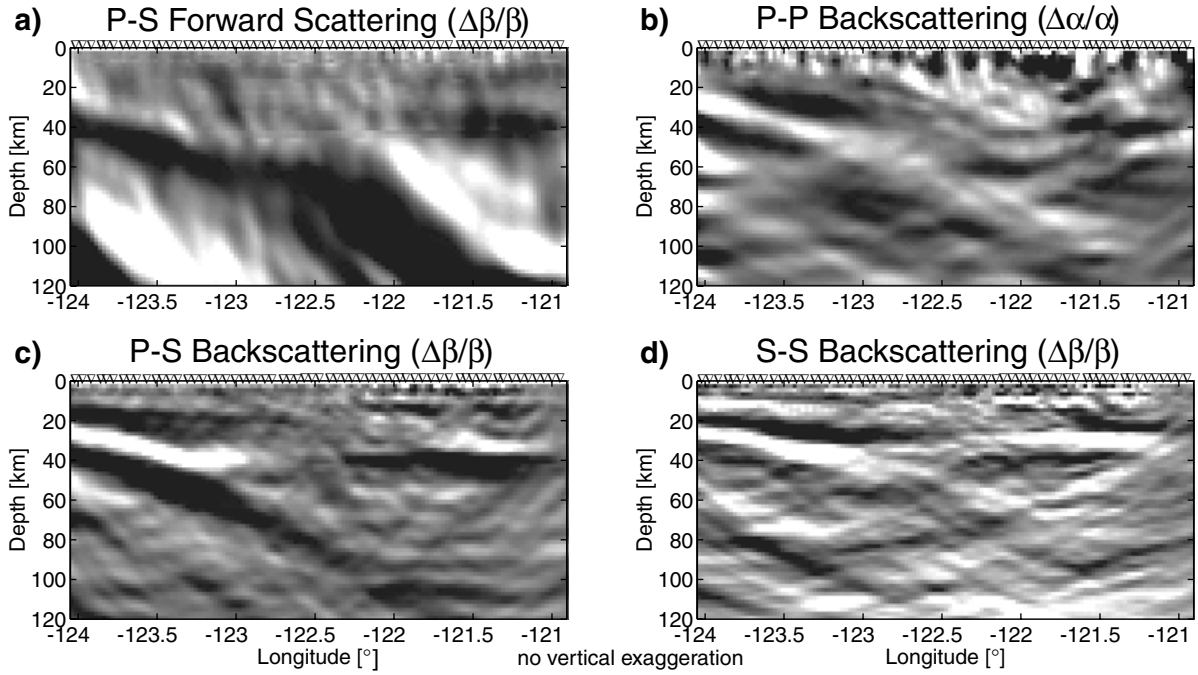

Figure 5. Results from single scattering-mode inversion of all events listed in Table 1. Gray scale is defined as for Figure 4. Note the improvement in resolution (e.g., confinement of the low-velocity dipping layer) with increasing sensitivity of total travel time to scatterer location, $\nabla \mathcal{T}^q$, from forward scattering to backscattering modes.

trolled source seismology [*Keach et al.*, 1989; *Tréhu et al.*, 1994].

4.6. Interpretation of the Low-Velocity Crustal Disruption

In this section, we investigate two possible interpretations for the disruption of oceanic crust and associated change in properties of the subducting slab (i.e., dip increase and weaker signature) apparent in the model of Plate 1. These interpretations are (see Figure 6) the delamination/underplating of the subducting crust resulting in tectonic layering and the entrapment of aqueous fluids released through metamorphic reactions in the subducting crust.

4.6.1. Delamination-tectonic layering. The first interpretation can be further subdivided into two contrasting classes of subduction structure on the basis of previous geophysical studies of subduction complexes: (1) underplating of sediments and/or mafic material from the oceanic crust to the accretionary wedge along the subduction décollement [*Green et al.*, 1986; *Clowes et al.*, 1987; *Hyndman et al.*, 1990; *Calvert and Clowes*, 1990; *Calvert*, 1996; *Keach et al.*, 1989; *Tréhu et al.*, 1994] and (2) continuous, large-scale delamination of the subducting crust [*Tsumura et al.*, 1999; A. Levander et al., Deformation, mass transfer, and crustal recycling at the Mendocino triple junction: What Gorda gives up, North America receives, submitted to *Tectonics*, 2000, hereinafter referred to as Levander et al., submitted manuscript, 2000].

Underplating of subducted materials to the accretionary prism was proposed for the northern Cascadia subduction zone, beneath Vancouver Island in several Lithoprobe studies [e.g., *Green et al.*, 1986; *Clowes et al.*, 1987; *Hyndman et al.*, 1990]. A ubiquitous reflector band labeled E was identified that runs subparallel to, and approximately ~5–10 km above, the present location of the subduction thrust plane (see *Hyndman et al.* [1990] for a review). The reflector band dips at a slightly lower angle than the subducting plate and eventually merges seaward into the interplate décollement [*Calvert*, 1996]. A second layer, labeled C, was intermittently imaged closer to the surface and separated from E by a low-reflectivity, high-velocity zone. One interpretation of this layering involves a succession of underplated marine sediments (reflective bands C and E) and accreted layers of oceanic crust and mantle (high-velocity/low-reflectivity zone). The underplating of sediments is postulated to operate continuously, whereas the accretion of crustal layers is envisaged as an episodic process associated with seaward jumps of the subduction zone. Similar accretionary mechanisms have been proposed for the tectonic regime in central Oregon on the basis of layering imaged from seismic reflection [*Keach et al.*, 1989] and refraction/wide-angle reflection [*Tréhu et al.*, 1994] studies. In this context, the apparent thickening and disruption of oceanic crust imaged here could represent a zone of continuously accumulated marine sediments or a discretely accreted fragment of oceanic crust [*Tréhu et al.*, 1994]. Both mechanisms can account for the observed geometry and velocity contrast; however, it appears implausible that either one could be fully responsible for the increase in slab dip and the diminished signature of the more deeply subducted crust. More specifically, the relative volume of removed material is small and unlikely to result in a significant change in buoyancy.

Large-scale delamination of the oceanic crust has been inferred from seismic studies of subduction zones in southernmost Cascadia (e.g., Levander et al., submitted manuscript, 2000) and Japan [*Tsumura et al.*, 1999]. In this scenario, a layer of slab material is separated from the underlying plate and directed either toward the surface (e.g., Hidaka Collision Zone [*Tsumura et al.*, 1999]) or into low-viscosity zones such as slab windows (e.g., southeast of the Mendocino Triple Junction (Levander et al., submitted manuscript, 2000)). In northern California (Levander et al., submitted manuscript, 2000) the Juan de Fuca plate is inferred

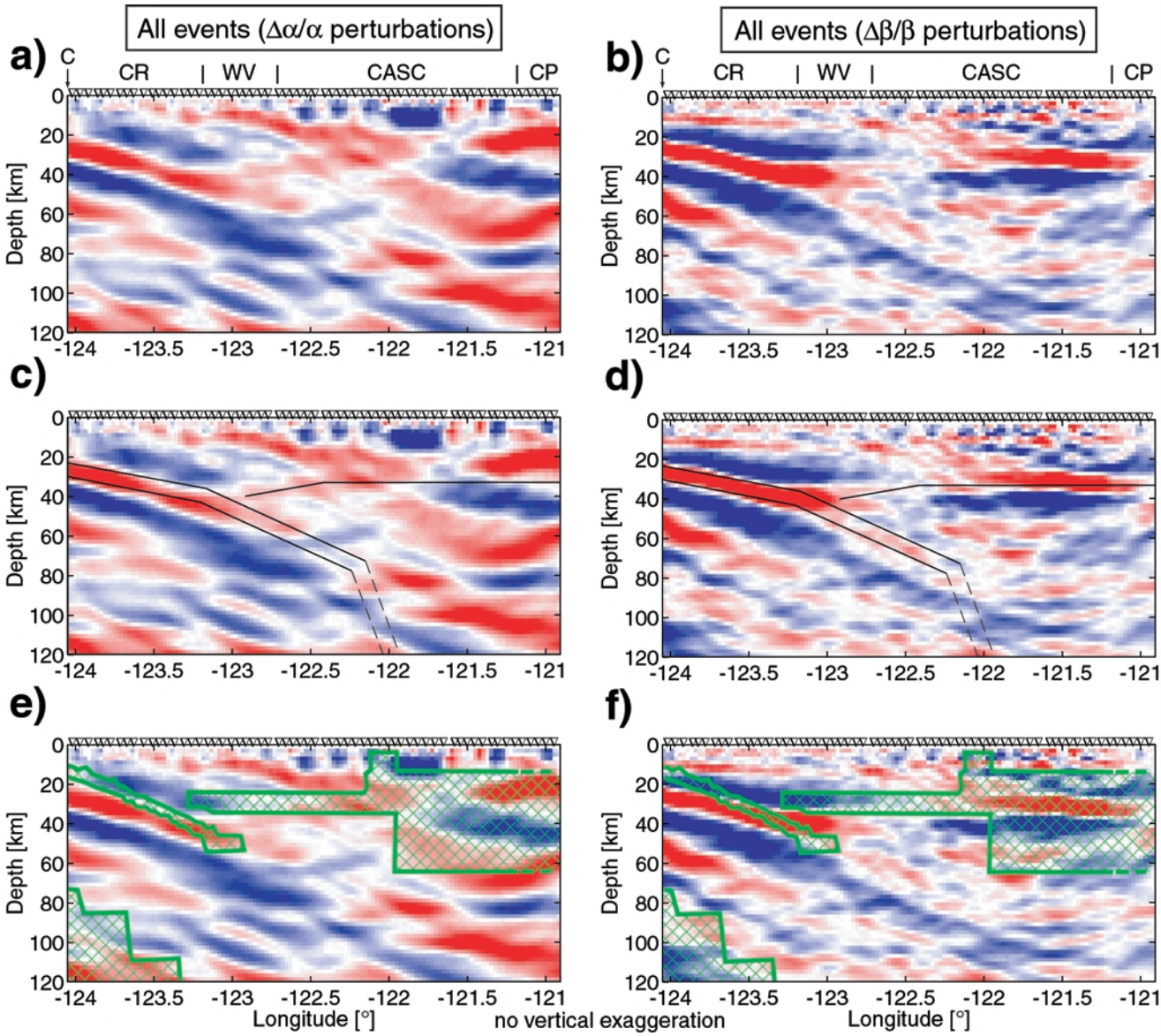

Plate 1. Results from simultaneous inversion of all events and scattering modes listed in Table 1: (a) *P* and (b) *S* velocity perturbation models, overlain by (c)–(d) contour of receiver function model by *Li* [1996] and (e)–(f) contour of conductive features (green) modeled by *Wannamaker et al.* [1989]. Color scale indicates slow (red) and fast (blue) velocity perturbations. The western edge of the model coincides with the coastline (C), and major physiographic units crossed by the receiver array are the Coast Ranges (CR), Willamette Valley (WV), Cascade Range (CASC), and Columbia Plateau (CP).

to enter the subduction zone with a slightly negative net buoyancy with respect to the continental upper mantle. However, upon separation of the crust the denser mantle portion of the plate sinks at a higher angle (Levander et al., submitted manuscript, 2000). This model can explain the increase in slab dip beneath the imaged crustal disruption; however, one might therefore expect the lower velocities to completely disappear beneath 40 km depth, which is not observed. Furthermore, there is no obvious outlet in central Oregon for the delaminated oceanic crust (i.e., no evidence for recently exhumed Juan de Fuca oceanic crust in the forearc) and no slab window into which the delaminated crust could feed. On this basis we discount the delamination model, and in section 4.6.2 we present a preferred explanation that also accommodates a range of other geophysical and geological observables.

4.6.2. Aqueous fluids and hydrated minerals. A growing body of petrological and geophysical evidence suggests that fluids and fluid migration play an important role in shallow subduction zone dynamics [*Kurtz et al.*, 1986; *Hyndman*, 1988; *Wannamaker et al.*, 1989; *Peacock*, 1996; *Hacker*, 1996; *ANCORP Working Group*, 1999; *Ernst*, 1999]. Recent petrological work [*Peacock*, 1996; *Hacker*, 1996; *Ernst*, 1999] emphasizes that significant dehydration at shallow subduction zone pressures and temperatures (P-T) results from prograde metamorphic reactions of hydrated minerals such as Na-amphibole and chlorite, contained primarily in altered basaltic and gabbroic layers of the crust. Maximum dehydration occurs through the blueschist-to-eclogite facies transition in most steady state subduction regimes [*Peacock*, 1996] but may also occur in a progressive fashion in younger/warmer subduction zones, such as Cascadia, where intermediate

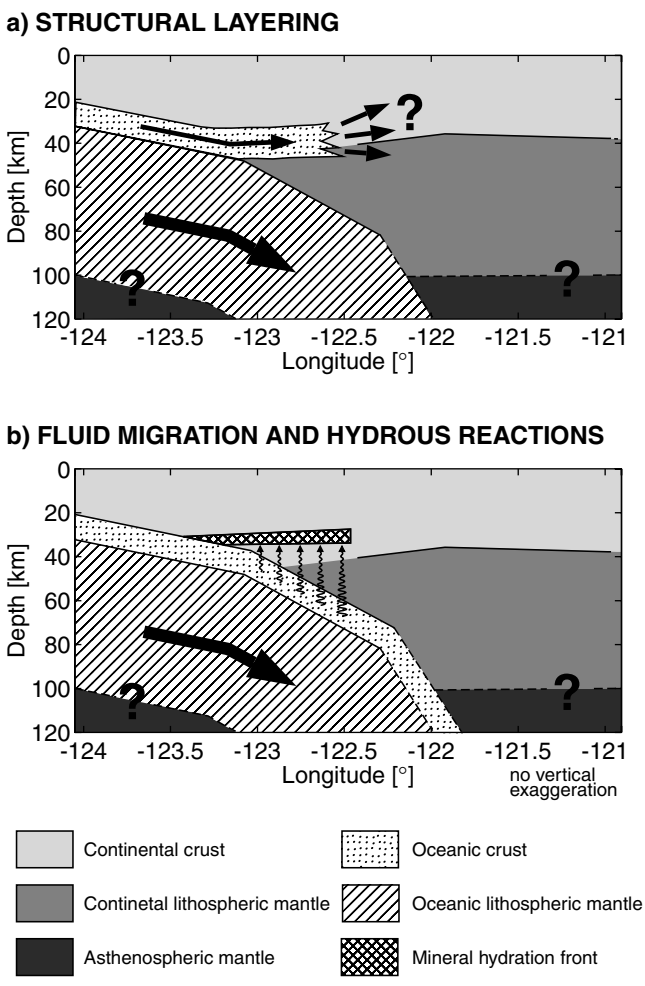

Figure 6. Schematic diagrams representing two possible interpretations for the crustal disruption imaged in Plate 1: (a) delamination of the oceanic crust and (b) dehydration/devolitilization of the oceanic crust and mineral reactions in the overriding wedge.

facies including greenschist, amphibolite, and granulite are likely to be encountered [*Hacker*, 1996]. Thermal models for the subduction regime in central Oregon [*Hyndman and Wang*, 1993; *Oleskevich et al.*, 1999] have been used to constrain temperatures along the main subduction décollement. Beneath the coast, the top of the crust is located at 20 km depth (~0.7 GPa) and has an estimated temperature of 450°C, corresponding to P-T conditions in the greenschist facies [e.g., *Hacker*, 1996]. At 40 km depth (~1.3 GPa) beneath the Willamette Valley, where the crustal disruption and other changes in slab properties are imaged, temperatures on the thrust plane are ~550–600°C, yielding P-T conditions that correspond to the amphibolite-to-eclogite facies transition.

A magnetotelluric study undertaken in northern Cascadia (Vancouver Island) by *Kurtz et al.* [1986] interpreted high-conductivity layering subparallel to the plate décollement in terms of subduction-entrained fluids. This layering, which coincides with the reflective band E discussed in section 4.6.1, was later interpreted by *Hyndman* [1988] as a concentration of fluids expelled from the oceanic crust as a result of dehydration. The fluids were inferred to migrate upward into the overriding lithospheric wedge where they encounter lower P-T conditions corresponding to retrograde facies transitions. Mineral hydration reactions can then occur, forming impermeable boundaries that trap fluids rising from below and produce high-conductivity/reflectivity anomalies in the subduction complex. *Hyndman* [1988] further suggested that progressive silica precipitation due to decreased solubility in rising fluids may also contribute to the formation of such impermeable boundaries.

A similar interpretation has been invoked by the EMSLAB Group [*Wannamaker et al.*, 1989] to explain a strong conductivity anomaly beneath central Oregon, in close proximity to the current study. Plates 1e and 1f show an outline of the resistivity model from *Wannamaker et al.* [1989] superimposed on our velocity perturbation model. Recognizing the nonuniqueness of resistivity models, especially in the vertical direction where only the conductance (conductivity-thickness product) of discrete layers can be resolved [*Wannamaker et al.*, 1989; *Jones*, 1993], there is reasonably good agreement between the dipping layers imaged by both techniques. We further note that the western limit of enhanced conductivity extending beneath the Willamette Valley and the Cascades, which has been interpreted by *Wannamaker et al.* [1989] as a zone of trapped fluids, coincides with the location of oceanic crustal thickening and disruption.

The foregoing studies motivate our preferred explanation for the structure shown in Plate 1 in terms of dehydration and eclogitization. Specifically, we interpret the apparent thickening of the oceanic crust and the shallowing of its upper boundary to manifest primarily the migration of fluids rather than structural changes within the crust per se. That is, dehydration reactions flux fluids into material above the oceanic crust, lowering its velocity and increasing its conductivity. The upper extent of this process is sharply defined by an impermeable boundary which merges seaward with the subduction décollement. This boundary may represent a retrograde metamorphic front, or it may be structurally controlled. Increased dip of the plate and reduced signature of the oceanic crust at greater depths imply that the dehydration reactions culminate in eclogitization with an accompanying density increase of 10–15% [*Hacker*, 1996]. The location, beneath the Willamette Valley, where the changes occur is, moreover, consistent with the hypothesis of *Rogers* [1983] that the density increase is also responsible for the development of trench-parallel lowlands (Willamette Valley, Puget Sound, Georgia Strait) in the Cascadia forearc.

5. Concluding Remarks

A new method for imaging detailed lithospheric structures using the teleseismic body wave coda has been developed in paper 1 of this series. In this paper, we have applied the method to a field data set collected over central Oregon and illustrated the contributions made by different scattering modes and source wave fields in the inversion procedure. We have demonstrated that the method can be used to reveal complex structures associated with dynamic processes in subduction zones. In particular, changes in the expression of the subducting Juan de Fuca plate have been related to dehydration and densification accompanying prograde metamorphic reactions in the oceanic crust. It is our hope that the success of this effort will provide motivation for new and ambitious experiments designed to exploit scattered, teleseismic body waves for the resolution of crust and mantle structure at finer scales than hitherto possible.

Acknowledgments. We are grateful to Rick Benson at the IRIS-DMC for his considerable efforts in providing us access to the CASC93 data set. We thank Alan Levander for sending us a preprint of his paper, Gary Pavlis and Justin Revenaugh for helpful reviews, and Joachim Saul for carefully verifying the equations. We acknowledge the efforts of John Nabelek and coworkers at Oregon State University in acquiring an exemplary data set. This work was supported by NSERC research grant OGP0138004.

References

ANCORP Working Group, Seismic reflection image revealing offset of Andean subduction-zone earthquake locations into oceanic mantle, *Nature*, *397*, 341–344, 1999.

Beylkin, G., Imaging of discontinuities in the inverse scattering problem by inversion of a causal generalized Radon transform, *J. Math. Phys.*, *26*, 99–108, 1985.

Beylkin, G., and R. Burridge, Linearized inverse scattering problem by inversion of a causal generalized Radon transform, *Wave Motion*, *12*, 15–52, 1990.

Bostock, M. G., Mantle stratigraphy and evolution of the Slave province, *J. Geophys. Res.*, *103*, 21,183–21,200, 1998.

Bostock, M. G., and S. Rondenay, Migration of scattered teleseismic body waves, *Geophys. J. Int.*, *137*, 732–746, 1999. (Corrigendum to "Migration of scattered teleseismic body waves," *Geophys. J. Int., 139*, 597, 1999).

Bostock, M. G., S. Rondenay, and J. Shragge, Multiparameter two-dimensional inversion of scattered teleseismic body waves, 1, Theory for oblique incidence, *J. Geophys. Res.*, this issue.

Calvert, A. J., Seismic reflection constraints on imbrication and underplating of the northern Cascadia convergent margin, *Can. J. Earth Sci.*, *33*, 1294–1307, 1996.

Calvert, A. J., and R. M. Clowes, Deep, high-amplitude reflections from a major shear zone above the subducting Juan de Fuca plate, *Geology*, *18*, 1091–1094, 1990.

Christiansen, R. L., S. R. Yeats, S. A. Graham, W. A. Niem, and D. P. Snavely, Post-Laramide geology of the U.S. Cordilleran region, in *The Geology of North America*, vol. G3, *The Cordilleran Orogen: Conterminous U.S.*, edited by C. B. Burchfiel, P. W. Lipman, and M. L. Zoback, pp. 261–406, Geol. Soc. of Am., Boulder, Colo., 1992.

Clowes, R. M., M. T. Brandon, A. G. Green, C. J. Yorath, A. Sutherland Brown, E. R. Kanasewich, and C. Spencer, Lithoprobe-southern Vancouver Island: Cenozoic subduction complex imaged by deep seismic reflections, *Can. J. Earth Sci.*, *24*, 31–51, 1987.

Couch, R. W., and R. P. Riddihough, The crustal structure of the western continental margin of North America, in *Geophysical Framework of the Continental United States*, edited by L. C. Pakiser and W. D. Mooney, *Mem. Geol. Soc. Am.*, *172*, 103–128, 1989.

DeMets, C., R. G. Gordon, D. F. Argus, and S. Stein, Current plate motions, *Geophys. J. Int.*, *101*, 423–478, 1990.

Dueker, K. G., and A. F. Sheehan, Mantle discontinuity structure from midpoint stacks of converted *P* to *S* waves across the Yellowstone hotspot track, *J. Geophys. Res.*, *102*, 8313–8327, 1997.

EMSLAB Group, The EMSLAB electromagnetic sounding experiment, *Eos Trans. AGU*, *69*(89), 98–99, 1988.

Ernst, W. G., Hornblende, the continent maker—Evolution of H_2O during circum-Pacific subduction versus continental collision, *Geology*, *27*, 675–678, 1999.

Fleming, S. W., and A. M. Tréhu, Crustal structure beneath the central Oregon convergent margin from potential-field modeling: Evidence for a buried basement ridge in local contact with a seaward dipping backstop, *J. Geophys. Res.*, *104*, 20,431–20,447, 1999.

Flueh, E. R., M. A. Fisher, J. Bialas, J. R. Childs, D. Klaeschen, N. Kukowski, T. Parsons, D. W. Scholl, U. ten Brink, A. M. Tréhu, and N. Vidal, New seismic images of the Cascadia subduction zone from cruise SO108-ORWELL, *Tectonophysics*, *293*, 69–84, 1998.

Forgues, E., and G. Lambaré, Parameterization study for acoustic and elastic ray + Born inversion, *J. Seismol. Explor.*, *6*, 253–277, 1997.

Green, A. G., R. M. Clowes, C. J. Yorath, C. Spencer, E. R. Kanasewich, M. T. Brandon, and A. Sutherland Brown, Seismic reflection imaging of the subducting Juan de Fuca plate, *Nature*, *319*, 210–213, 1986.

Hacker, B. R., Eclogite formation and rheology, buoyancy, seismicity, and H_2O content of oceanic crust, in *Subduction: Top to Bottom, Geophys. Monogr. Ser.*, vol. 96, edited by E. G. Bebout et al., pp. 337–346, AGU, Washington, D. C., 1996.

Harris, R. A., H. M. Iyer, and P. B. Dawson, Imaging the Juan de Fuca plate beneath southern Oregon using teleseismic *P* wave residuals, *J. Geophys. Res.*, *96*, 19,879–19,889, 1991.

Heaton, T. H., and S. H. Hartzell, Earthquake hazards on the Cascadia subduction zone, *Science*, *236*, 162–168, 1987.

Holbrook, W. S., W. D. Mooney, and N. I. Christensen, The seismic velocity structure of the deep continental crust, in *Continental Lower Crust*, edited by D. M. Fountain, R. Arculus, and R. W. Kay, pp. 1–34, Elsevier Sci., New York, 1992.

Hyndman, R. D., Dipping seismic reflectors, electrically conductive zones, and trapped water in the crust over a subducting plate, *J. Geophys. Res.*, *93*, 13,391–13,405, 1988.

Hyndman, R. D., and K. Wang, Thermal constraints on the zone of major thrust earthquake failure: The Cascadia subduction zone, *J. Geophys. Res.*, *98*, 2039–2060, 1993.

Hyndman, R. D., C. J. Yorath, R. M. Clowes, and E. E. Davis, The northern Cascadia subduction zone at Vancouver Island: Seismic structure and tectonic history, *Can. J. Earth Sci.*, *27*, 313–329, 1990.

Jones, A. G., Electromagnetic images of modern and ancient subduction zones, *Tectonophysics*, *219*, 29–45, 1993.

Keach, R. W., J. E. Oliver, L. D. Brown, and S. Kaufman, Cenozoic active margin and shallow Cascades structure: COCORP results from western Oregon, *Geol. Soc. Am. Bull.*, *101*, 783–794, 1989.

Kennett, B. L. N., The removal of free surface interactions from three-component seismograms, *Geophys. J. Int.*, *104*, 153–163, 1991.

Kurtz, R. M., J. M. DeLaurier, and J. C. Gupta, A magnetotelluric sounding across Vancouver Island detects the subducting Juan de Fuca plate, *Nature*, *321*, 596–599, 1986.

Langston, C. A., Structure under Mount Rainier, Washington, inferred from teleseismic body waves, *J. Geophys. Res.*, *84*, 4749–4762, 1979.

Langston, C. A., Evidence for the subducting lithosphere under southern Vancouver Island and western Oregon from teleseismic *P* wave conversions, *J. Geophys. Res.*, *86*, 3857–3866, 1981.

Li, X.-Q., Deconvolving orbital surface waves for the source duration of large earthquakes and modeling the receiver functions for the earth structure beneath a broadband seismometer array in the Cascadia subduction zone, Ph.D. thesis, 153 pp., Oreg. State Univ., Corvallis, Sept. 1996.

Michaelson, C. A., and C. S. Weaver, Upper mantle structure from teleseismic *P* wave arrivals in Washington and northern Oregon, *J. Geophys. Res.*, *91*, 2077–2094, 1986.

Mooney, W. D., and C. S. Weaver, Regional crustal structure and tectonics of the Pacific coastal states: California, Oregon, and Washington, in *Geophysical Framework of the Continental United States*, edited by L. C. Pakiser and W. D. Mooney, *Mem. Geol. Soc. Am.*, *172*, 129–161, 1989.

Nabelek, J., X.-Q. Li, S. Azevedo, J. Braunmiller, A. Fabritius, B. Leitner, A. M. Tréhu, and G. Zandt, A high-resolution image of the Cascadia subduction zone from teleseismic converted phases recorded by a broadband seismic array, *Eos Trans. AGU*, *74*(43), Fall Meet. Suppl., 431, 1993.

Oleskevich, D. A., R. D. Hyndman, and K. Wang, The updip and downdip limits to great subduction earthquakes: Thermal and structural models of Cascadia, south Alaska, SW Japan, and Chile, *J. Geophys. Res.*, *104*, 14,965–14,991, 1999.

Owens, T. J., G. Zandt, and S. R. Taylor, Seismic evidence from an ancient rift beneath the Cumberland Plateau, Tennessee: A detailed analysis of broadband teleseismic *P* waveforms, *J. Geophys. Res.*, *89*, 7783–7795, 1984.

Peacock, S. M., Thermal and petrologic structure of subduction zones, in *Subduction: Top to Bottom, Geophys. Monogr. Ser.*, vol. 96, edited by E. G. Bebout et al., pp. 119–133, AGU, Washington, D. C., 1996.

Rasmussen, J., and E. Humphreys, Tomographic image of the Juan de Fuca plate beneath Washington and western Oregon using teleseismic *P*-wave travel times, *Geophys. Res. Lett.*, *15*, 1417–1420, 1988.

Revenaugh, J., A scattered-wave image of subduction beneath the Transverse Ranges, *Science*, *268*, 1888–1892, 1995.

Revenaugh, J., and T. H. Jordan, Mantle layering from *ScS* reverberations, 3, The upper mantle, *J. Geophys. Res.*, *96*, 19,781–19,810, 1991.

Rogers, G. C., Seismotectonics of British Columbia, Ph.D. thesis, 247 pp., Univ. of British Columbia, Vancouver, Canada, Jan. 1983.

Ryberg, T., and M. Weber, Receiver function arrays: A reflection seismic approach, *Geophys. J. Int.*, *141*, 1–11, 2000.

Sheehan, A. F., P. M. Shearer, H. J. Gilbert, and K. G. Dueker, Seismic migration processing of *P-SV* converted phases for mantle discontinuity structure beneath the Snake River Plain, western United States, *J. Geophys. Res.*, *105*, 19,055–19,065, 2000.

Shragge, J., M. G. Bostock, and S. Rondenay, Multiparameter two-dimensional inversion of scattered teleseismic body waves, 2, Numerical examples, *J. Geophys. Res.*, this issue.

Tréhu, A. M., I. Asudeh, T. M. Brocher, J. H. Luetgert, W. D. Mooney, J. L. Nabelek, and Y. Nakamura, Crustal architecture of the Cascadia forearc, *Science*, *266*, 237–243, 1994.

Tsumura, N., H. Ikawa, T. Ikawa, M. Shinohara, T. Ito, K. Arita, T. Moriya, G. Kimura, and T. Ikawa, Delamination-wedge structure beneath the Hidaka collision zone, central Hokkaido, Japan inferred from seismic reflection profiling, *Geophys. Res. Lett.*, *26*, 1057–1060, 1999.

Ulrych, T. J., S. L. M. Freire, and M. D. Sacchi, Eigenimage processing of seismic sections, in *Covariance Analysis for Seismic Signal Processing*, edited by R. L. Kirlin and W. J. Done, pp. 241–274, Soc. of Explor. Geophys., Tulsa, Okla., 1999.

VanDecar, J. C., Upper-mantle structure of the Cascadia subduction zone

from non-linear teleseismic travel-time inversion, Ph.D. thesis, 165 pp., Univ. of Wash., Seattle, June 1991.

VanDecar, J. C., and R. S. Crosson, Determination of teleseismic relative phase arrival times using multi-channel cross-correlation and least squares, *Bull. Seismol. Soc. Am.*, *80*, 150–159, 1990.

Wannamaker, P. E., J. R. Booker, A. G. Jones, A. D. Chave, J. H. Filloux, H. S. Waff, and L. K. Law, Resistivity cross section through the Juan de Fuca subduction system and its tectonic implications, *J. Geophys. Res.*, *94*, 14,127–14,144, 1989.

Weaver, C. S., and C. A. Michaelson, Seismicity and volcanism in the Pacific Northwest: evidence for the segmentation of the Juan de Fuca plate, *Geophys. Res. Lett.*, *12*, 215–218, 1985.

M. G. Bostock, Department of Earth and Ocean Sciences, University of British Columbia, 129-2219 Main Mall, Vancouver, British Columbia, Canada, V6T 1Z4. (bostock@geop.ubc.ca)

S. Rondenay, Department of Geological Sciences, Brown University, Dept. Box 1846, Providence, RI 02912, USA. (rondenay@emma.geo.brown.edu)

J. Shragge, Hager GeoScience Inc., 596 Main Street, Woburn, MA 01801, USA.

(Received October 31, 2000; revised July 13, 2001;
accepted July 18, 2001.)